

# Dimers, trimers, tetramers, and other multimers in a multiband Bose-Hubbard model

M. Iskin<sup>1</sup> and A. Keleş<sup>2</sup>

<sup>1</sup>*Department of Physics, Koç University, Rumelifeneri Yolu, 34450 Sarıyer, Istanbul, Turkey*

<sup>2</sup>*Department of Physics, Middle East Technical University, Ankara, 06800, Turkey*

(Dated: August 3, 2022)

We study the bound states of  $N$  identical bosons that are described by a multiband Bose-Hubbard model with generic hoppings and an attractive onsite interaction. Using a variational approach, we first derive exact integral equations for the dimers, trimers, tetramers, and other multimers, and then apply them to a one-dimensional sawtooth model that features two bands. In particular we reveal the presence of not only the offsite dimer states which consist of two monomers on different sites even in the strong-coupling limit but also the offsite trimer states which consist of either a dimer on one site and a monomer on another site or three monomers on three different sites. Our variational calculations for the ground states of onsite dimers, onsite trimers and offsite trimers benchmark perfectly well with the DMRG simulations. We also present DMRG results for the ground states of onsite tetramers, offsite tetramers, onsite pentamers, offsite pentamers, and for those of other multimers.

## I. INTRODUCTION

Exactly solvable few-body problems [1], including but not limited to dimers, trimers and tetramers, in a periodic lattice have long been of interest to physicists in the contexts of Cooper pairs in superconductors, excitons and Frenkel-exciton-hole trions in semiconductors, multimagnons in quantum magnetism, Efimov trimers in BECs and other quantum gases/liquids, etc. However, since almost all of the studies in the literature are about single-band lattices, the effects of multiple bands have entirely been overlooked. For instance while dimers have long been known to be the only possible bound state between identical (i.e., equal-mass) fermions in a single-band lattice [1], the energetic stability of trimers, tetramers and some other multimers have recently been shown in the presence of multiple Bloch bands [2–4]. It is conceivable that there may not even be an upper bound on the size of the possible multimers when they are formed in a flat band, albeit with smaller and smaller binding energies [4].

On the other hand dimers, trimers, tetramers and all other multimers have long been known to be allowed for identical bosons in a single-band lattice due to the absence of Pauli exclusion [1]. Except for the dimers, these states form discontinuously in three dimensions (i.e., they have finite size at the formation threshold) as a function of interaction strength, so that they are already in the strong-coupling regime when they appear and are strongly co-localized on the same lattice site. They are sometimes called the onsite trimers, onsite tetramers, etc., since their binding energies are linearly proportional to the interaction strength in the strong-coupling limit just like those of the onsite dimers [5–7]. Onsite trimers form continuously in lower (two and one) dimensions without a threshold on the coupling strength. Remarkably there are also weakly-bound offsite trimer states (above the ground state of the spectrum in the strong-coupling limit) which consist of a dimer on one site and a monomer on another site, and whose peculiar

binding mechanism turns out to be an effective particle-exchange interaction between the onsite dimer and the monomer [8].

In this paper we study the effects of multiple Bloch bands on the formation of few-boson bound states. For this purpose we first derive exact integral equations for the dimers, trimers, tetramers, and other multimers that are described by a multiband Bose-Hubbard model with generic hoppings and an onsite attractive interaction. Then, motivated primarily by our benchmarking capacity with the DMRG simulations, we calculate the two-body and three-body spectra in a one-dimensional sawtooth model that features two Bloch bands. One of our main findings is that, in addition to the onsite dimer, onsite trimer and offsite trimer states, the two-band lattice also exhibits weakly-bound offsite dimer states which consist of two monomers on different sites even in the strong-coupling limit. In return these offsite dimers also give rise to offsite trimers that consist of three monomers on three different sites in the strong-coupling limit. We show that our results for the ground states of onsite dimers, onsite trimers and offsite trimers perfectly benchmark with the DMRG simulations, and we present additional DMRG results for the ground states of onsite tetramers, offsite tetramers, onsite pentamers, offsite pentamers and for those of other multimers. Given that our variational results are readily applicable to all sorts of lattices in all dimensions, we believe they may find useful applications in future few-body studies.

The rest of the paper is organized as follows. In Sec. II we first introduce the Hamiltonian for the multiband Bose-Hubbard model in reciprocal space, and then use the variational approach to derive integral equations for the  $N$ -body bound states, including the dimers ( $N = 2$ ), trimers ( $N = 3$ ), tetramers ( $N = 4$ ), and other multimers ( $N \geq 5$ ). In Sec. III we apply our theory to a sawtooth lattice, analyze the full dimer and trimer spectra, and benchmark them with the DMRG simulations. The paper ends with a brief summary of our findings and outlook in Sec. IV.

## II. VARIATIONAL APPROACH

Motivated by the success of variational approach in describing the few-fermion bound states in a multiband Hubbard model [4], here we extend it to study the few-boson bound states in a multiband Bose-Hubbard model.

### A. Multiband Bose-Hubbard model

The Bose-Hubbard model [9] and its various extensions are often employed in the analysis of the low-temperature phases of cold bosonic atoms in optical lattices but not limited to them. Historically the observation of superfluid-Mott insulator transition was one of the most prominent achievements in this field. See, e.g., Refs. [10–13] and many others. In its simplest form, the model Hamiltonian can be written as

$$\mathcal{H} = - \sum_{S_i, S'_i} t_{S_i, S'_i} c_{S_i}^\dagger c_{S'_i} + \frac{U}{2} \sum_{S_i} c_{S_i}^\dagger c_{S_i}^\dagger c_{S_i} c_{S_i}, \quad (1)$$

where the first term accounts for the hopping of particles from a site  $S'$  in unit cell  $i'$  to a site  $S$  in unit cell  $i$  with amplitude  $t_{S_i, S'_i}$ , and the second term accounts for the density-density interaction between particles when they are on the same site. Here a positive or negative  $U$  corresponds, respectively, to a repulsive or attractive interaction, and the prefactor  $1/2$  is to avoid double counting. In this paper we have a generic lattice with periodic boundary conditions in mind, where  $N_c$  is the number of unit cells in the system and  $N_b$  is the number of sublattices in a given unit cell. This is in such a way that the total number of lattice sites in the system is  $N_s = N_b N_c$ .

In reciprocal space, the Bose-Hubbard model can be conveniently expressed as [14]

$$\begin{aligned} \mathcal{H} = & \sum_{n\mathbf{k}} \varepsilon_{n\mathbf{k}} c_{n\mathbf{k}}^\dagger c_{n\mathbf{k}} + \frac{1}{2N_c} \sum_{\substack{nmn'm' \\ \mathbf{k}\mathbf{k}'\mathbf{q}}} V_{n'm'\mathbf{k}'}^{nm\mathbf{k}}(\mathbf{q}) \\ & \times c_{n, \mathbf{k}+\frac{\mathbf{q}}{2}}^\dagger c_{m, -\mathbf{k}+\frac{\mathbf{q}}{2}}^\dagger c_{m', -\mathbf{k}'+\frac{\mathbf{q}}{2}} c_{n', \mathbf{k}'+\frac{\mathbf{q}}{2}}, \quad (2) \end{aligned}$$

where  $n$  denotes the Bloch bands,  $\mathbf{k}$  is the crystal momentum in the first Brillouin zone (BZ),  $\varepsilon_{n\mathbf{k}}$  is the corresponding single-particle dispersion, and  $V_{n'm'\mathbf{k}'}^{nm\mathbf{k}}(\mathbf{q}) = U \sum_S n_{S, \mathbf{k}+\frac{\mathbf{q}}{2}}^* m_{S, -\mathbf{k}+\frac{\mathbf{q}}{2}}^* m'_{S, -\mathbf{k}'+\frac{\mathbf{q}}{2}} n'_{S, \mathbf{k}'+\frac{\mathbf{q}}{2}}$  characterizes the onsite interactions. This Hamiltonian simply follows from the Fourier expansion  $c_{S_i}^\dagger = \frac{1}{\sqrt{N_c}} \sum_{\mathbf{k}} e^{-i\mathbf{k}\cdot\mathbf{r}_{S_i}} c_{S\mathbf{k}}^\dagger$  of the site operators where  $\mathbf{r}_{S_i}$  is the position of the sublattice site  $S$  in unit cell  $i$ , along with the basis transformation  $c_{n\mathbf{k}}^\dagger = \sum_S n_{S\mathbf{k}} c_{S\mathbf{k}}^\dagger$  where  $n_{S\mathbf{k}}$  is the projection of the Bloch state onto the sublattice  $S$ . Note that there are  $N_b$  Bloch bands for a system that

has  $N_b$  sublattices in its unit cell. In this paper we are interested in the bound states of  $N$  identical bosons that are described by Eq. (2).

### B. $N$ -body bound states

For a given center-of-mass (CoM) momentum  $\mathbf{q}$ , the energy  $E_N^{\mathbf{q}}$  of an  $N$ -body bound state  $|\Psi_{\mathbf{q}}\rangle$  follows from the Schrödinger equation  $\mathcal{H}|\Psi_{\mathbf{q}}\rangle = E_N^{\mathbf{q}}|\Psi_{\mathbf{q}}\rangle$ . In our variational approach, these bound states are described exactly by the ansatz

$$|\Psi_{\mathbf{q}}\rangle = \sum_{\substack{n_1 \cdots n_N \\ \mathbf{k}_1 \cdots \mathbf{k}_{N-1}}} \alpha_{n_1 \cdots n_{N-1} n_N}^{\mathbf{k}_1 \cdots \mathbf{k}_{N-1}}(\mathbf{q}) \left( \prod_{i=1}^N c_{n_i \mathbf{k}_i}^\dagger \right) |0\rangle, \quad (3)$$

where the variational parameter  $\alpha_{n_1 \cdots n_{N-1} n_N}^{\mathbf{k}_1 \cdots \mathbf{k}_{N-1}}(\mathbf{q})$  is a complex number that depends on all of the band as well as momentum indices with the exception of  $\mathbf{k}_N$ . This is because  $\mathbf{k}_N = \mathbf{q} - \sum_{i=1}^{N-1} \mathbf{k}_i$  follows from the conservation of  $\mathbf{q}$ , and it is not an independent variable. The normalization condition can be written as  $\langle \Psi_{\mathbf{q}} | \Psi_{\mathbf{q}} \rangle = N! \sum_{\mathbf{k}_1 \cdots \mathbf{k}_{N-1}} |\alpha_{n_1 \cdots n_{N-1} n_N}^{\mathbf{k}_1 \cdots \mathbf{k}_{N-1}}(\mathbf{q})|^2$ , where we make extensive use of the relations

$$\alpha_{n_1 \cdots n_i \cdots n_j \cdots n_{N-1} n_N}^{\mathbf{k}_1 \cdots \mathbf{k}_i \cdots \mathbf{k}_j \cdots \mathbf{k}_{N-1}}(\mathbf{q}) = \alpha_{n_1 \cdots n_j \cdots n_i \cdots n_{N-1} n_N}^{\mathbf{k}_1 \cdots \mathbf{k}_j \cdots \mathbf{k}_i \cdots \mathbf{k}_{N-1}}(\mathbf{q}), \quad (4)$$

$$\alpha_{n_1 \cdots n_i \cdots n_{N-1} n_N}^{\mathbf{k}_1 \cdots \mathbf{k}_i \cdots \mathbf{k}_{N-1}}(\mathbf{q}) = \alpha_{n_1 \cdots n_N \cdots n_{N-1} n_i}^{\mathbf{k}_1 \cdots \mathbf{k}_N \cdots \mathbf{k}_{N-1}}(\mathbf{q}), \quad (5)$$

that follow from the exchange symmetry of identical bosons.

After a lengthy but straightforward algebra, the expectation value of the Hamiltonian given in Eq. (2) can be written as

$$\begin{aligned} \langle \mathcal{H} \rangle = & N! \sum_{\substack{n_1 \cdots n_{N-1} n_N \\ \mathbf{k}_1 \cdots \mathbf{k}_{N-1}}} |\alpha_{n_1 \cdots n_{N-1} n_N}^{\mathbf{k}_1 \cdots \mathbf{k}_{N-1}}(\mathbf{q})|^2 \left( \sum_{i=1}^N \varepsilon_{n_i \mathbf{k}_i} \right) \\ & + N(N-1) \frac{U}{2N_c} \sum_{\substack{n_1 \cdots n_N m_1 m_2 \\ S \mathbf{k}_1 \cdots \mathbf{k}_{N-1} \mathbf{k}}} \alpha_{n_1 \cdots n_{N-1} n_N}^{\mathbf{k}_1 \cdots \mathbf{k}_{N-1}}(\mathbf{q}) m_{1S\mathbf{k}}^* \\ & \times \sum_P [\alpha_{n_{i_1} \cdots n_{i_{N-2}} m_1 m_2}^{\mathbf{k}_{i_1} \cdots \mathbf{k}_{i_{N-2}} \mathbf{k}}(\mathbf{q})]^* m_{2S\mathbf{Q}}^* n_{i_{N-1} S \mathbf{k}_{i_{N-1}}} n_{i_N S \mathbf{k}_{i_N}}. \quad (6) \end{aligned}$$

Here we define  $\mathbf{Q} = \mathbf{q} - \sum_{j=1}^{N-2} \mathbf{k}_{i_j} - \mathbf{k}$  for convenience, and the summation over  $P$  denotes all possible permutations of  $\{i_1, i_2, \dots, i_{N-1}\}$  subindices where each subindex refers to one of the  $N$  values in the set  $\{1, 2, \dots, N\}$ . This is such that  $\mathbf{k}_{i_j} \in \{\mathbf{k}_1, \mathbf{k}_2, \dots, \mathbf{k}_N\}$  and  $n_{i_j} \in \{n_1, n_2, \dots, n_N\}$ , respectively, span the corresponding momentum and band variables. The variational parameters are determined through the functional minimization of  $\langle \Psi_{\mathbf{q}} | \mathcal{H} - E_N^{\mathbf{q}} | \Psi_{\mathbf{q}} \rangle$ , leading eventually to

$$\gamma_{n_1 \dots n_{N-2} S}^{\mathbf{k}_1 \dots \mathbf{k}_{N-2}}(\mathbf{q}) = -\frac{N(N-1)}{N!} \frac{U}{2N_c} \sum_{n_{N-1} n_N S' \mathbf{k}_{N-1}} \frac{n_{N-1} S \mathbf{k}_{N-1} n_N S \mathbf{k}_N}{\left(\sum_{i=1}^N \varepsilon_{n_i \mathbf{k}_i}\right) - E_N^{\mathbf{q}}} \sum_P n_{i_{N-1} S' \mathbf{k}_{i_{N-1}}}^* n_{i_N S' \mathbf{k}_{i_N}}^* \gamma_{n_{i_1} \dots n_{i_{N-2}} S'}^{\mathbf{k}_{i_1} \dots \mathbf{k}_{i_{N-2}}}(\mathbf{q}), \quad (7)$$

where we define a renormalized parameter set  $\gamma_{n_1 \dots n_{N-2} S}^{\mathbf{k}_1 \dots \mathbf{k}_{N-2}}(\mathbf{q}) = \sum_{n_{N-1} n_N \mathbf{k}_{N-1}} \alpha_{n_1 \dots n_{N-1} n_N}^{\mathbf{k}_1 \dots \mathbf{k}_{N-1}}(\mathbf{q}) n_{N-1} S \mathbf{k}_{N-1} n_N S \mathbf{k}_N$  for convenience. We emphasize that Eq. (7) is formally exact for any  $N \geq 2$ , and it is one of our central results in this work.

For a given  $N$ , it is possible to reduce Eq. (7) to a much simpler form by making extensive use of the relation  $\gamma_{n_1 \dots n_i \dots n_j \dots n_{N-2} S}^{\mathbf{k}_1 \dots \mathbf{k}_i \dots \mathbf{k}_j \dots \mathbf{k}_{N-2}}(\mathbf{q}) = \gamma_{n_1 \dots n_j \dots n_i \dots n_{N-2} S}^{\mathbf{k}_1 \dots \mathbf{k}_j \dots \mathbf{k}_i \dots \mathbf{k}_{N-2}}(\mathbf{q})$  that follow from the exchange symmetry of identical bosons. For instance when  $N = 2$ , Eq. (7) reduces to

$$\gamma_S(\mathbf{q}) = -\frac{U}{N_c} \sum_{n_1 n_2 S' \mathbf{k}_1} \frac{n_1 S \mathbf{k}_1 n_2 S \mathbf{k}_2 n_1^* S' \mathbf{k}_1 n_2^* S' \mathbf{k}_2}{\varepsilon_{n_1 \mathbf{k}_1} + \varepsilon_{n_2 \mathbf{k}_2} - E_2^{\mathbf{q}}} \gamma_{S'}(\mathbf{q}), \quad (8)$$

where  $\mathbf{k}_2 = \mathbf{q} - \mathbf{k}_1$ . We note that this expression looks very similar (in fact formally identical) to that of the two-body bound states of fermions [2, 14]. In addition it recovers the single-band result [6, 7] when the band and sublattice indices are dropped from the summation, and the Bloch factors set to unity in the numerator. Similarly when  $N = 3$ , Eq. (7) reduces to

$$\begin{aligned} \gamma_{n_1 S}^{\mathbf{k}_1}(\mathbf{q}) &= -\frac{U}{N_c} \sum_{n_2 n_3 S' \mathbf{k}_2} \frac{n_2 S \mathbf{k}_2 n_3 S \mathbf{k}_3}{\left(\sum_{i=1}^3 \varepsilon_{n_i \mathbf{k}_i}\right) - E_3^{\mathbf{q}}} \quad (9) \\ &\times \left[ n_2^* S' \mathbf{k}_2 n_3^* S' \mathbf{k}_3 \gamma_{n_1 S'}^{\mathbf{k}_1}(\mathbf{q}) + n_1^* S' \mathbf{k}_1 n_3^* S' \mathbf{k}_3 \gamma_{n_2 S'}^{\mathbf{k}_2}(\mathbf{q}) \right. \\ &\quad \left. + n_1^* S' \mathbf{k}_1 n_2^* S' \mathbf{k}_2 \gamma_{n_3 S'}^{\mathbf{k}_3}(\mathbf{q}) \right], \end{aligned}$$

where  $\mathbf{k}_3 = \mathbf{q} - \mathbf{k}_1 - \mathbf{k}_2$ . Upon a change of the summation variable  $\mathbf{k}_2$ , it can be shown that the second and third terms in the square bracket have exactly the same contribution after the summations. Thus Eq. (9) can be equivalently written as

$$\begin{aligned} \gamma_{n_1 S}^{\mathbf{k}_1}(\mathbf{q}) &= -\frac{U}{N_c} \sum_{n_2 n_3 S' \mathbf{k}_2} \frac{n_2 S \mathbf{k}_2 n_3 S \mathbf{k}_3}{\left(\sum_{i=1}^3 \varepsilon_{n_i \mathbf{k}_i}\right) - E_3^{\mathbf{q}}} \quad (10) \\ &\times \left[ n_2^* S' \mathbf{k}_2 n_3^* S' \mathbf{k}_3 \gamma_{n_1 S'}^{\mathbf{k}_1}(\mathbf{q}) + 2n_1^* S' \mathbf{k}_1 n_3^* S' \mathbf{k}_3 \gamma_{n_2 S'}^{\mathbf{k}_2}(\mathbf{q}) \right]. \end{aligned}$$

Note that this expression also recovers the single-band result [1, 8] when the band and sublattice indices are dropped from the summation, and the Bloch factors set to unity. Furthermore when  $N = 4$ , Eq. (7) reduces to

$$\begin{aligned} \gamma_{n_1 n_2 S}^{\mathbf{k}_1 \mathbf{k}_2}(\mathbf{q}) &= -\frac{U}{N_c} \sum_{n_3 n_4 S' \mathbf{k}_3} \frac{n_3 S \mathbf{k}_3 n_4 S \mathbf{k}_4}{\left(\sum_{i=1}^4 \varepsilon_{n_i \mathbf{k}_i}\right) - E_4^{\mathbf{q}}} \quad (11) \\ &\times \left[ n_3^* S' \mathbf{k}_3 n_4^* S' \mathbf{k}_4 \gamma_{n_1 n_2 S'}^{\mathbf{k}_1 \mathbf{k}_2}(\mathbf{q}) + n_2^* S' \mathbf{k}_2 n_4^* S' \mathbf{k}_4 \gamma_{n_1 n_3 S'}^{\mathbf{k}_1 \mathbf{k}_3}(\mathbf{q}) \right. \\ &+ n_2^* S' \mathbf{k}_2 n_3^* S' \mathbf{k}_3 \gamma_{n_1 n_4 S'}^{\mathbf{k}_1 \mathbf{k}_4}(\mathbf{q}) + n_1^* S' \mathbf{k}_1 n_4^* S' \mathbf{k}_4 \gamma_{n_2 n_3 S'}^{\mathbf{k}_2 \mathbf{k}_3}(\mathbf{q}) \\ &\left. + n_1^* S' \mathbf{k}_1 n_3^* S' \mathbf{k}_3 \gamma_{n_2 n_4 S'}^{\mathbf{k}_2 \mathbf{k}_4}(\mathbf{q}) + n_1^* S' \mathbf{k}_1 n_2^* S' \mathbf{k}_2 \gamma_{n_3 n_4 S'}^{\mathbf{k}_3 \mathbf{k}_4}(\mathbf{q}) \right], \end{aligned}$$

where  $\mathbf{k}_4 = \mathbf{q} - \mathbf{k}_1 - \mathbf{k}_2 - \mathbf{k}_3$ . We again note that this expression recovers the single-band result [15] when the band and sublattice indices are dropped from the summation, and the Bloch factors set to unity. Moreover, upon a change of the summation variable  $\mathbf{k}_3$ , it can be shown that the second and third terms as well as the fourth and fifth terms in the square bracket have exactly the same contributions after the summations. Thus Eq. (11) can be equivalently written as

$$\begin{aligned} \gamma_{n_1 n_2 S}^{\mathbf{k}_1 \mathbf{k}_2}(\mathbf{q}) &= -\frac{U}{N_c} \sum_{n_3 n_4 S' \mathbf{k}_3} \frac{n_3 S \mathbf{k}_3 n_4 S \mathbf{k}_4}{\left(\sum_{i=1}^4 \varepsilon_{n_i \mathbf{k}_i}\right) - E_4^{\mathbf{q}}} \quad (12) \\ &\times \left[ n_3^* S' \mathbf{k}_3 n_4^* S' \mathbf{k}_4 \gamma_{n_1 n_2 S'}^{\mathbf{k}_1 \mathbf{k}_2}(\mathbf{q}) + 2n_2^* S' \mathbf{k}_2 n_4^* S' \mathbf{k}_4 \gamma_{n_1 n_3 S'}^{\mathbf{k}_1 \mathbf{k}_3}(\mathbf{q}) \right. \\ &\left. + 2n_1^* S' \mathbf{k}_1 n_4^* S' \mathbf{k}_4 \gamma_{n_2 n_3 S'}^{\mathbf{k}_2 \mathbf{k}_3}(\mathbf{q}) + n_1^* S' \mathbf{k}_1 n_2^* S' \mathbf{k}_2 \gamma_{n_3 n_4 S'}^{\mathbf{k}_3 \mathbf{k}_4}(\mathbf{q}) \right]. \end{aligned}$$

By following a similar strategy, Eq. (7) can be used to deduce the relevant integral equations for all other multimers with  $N \geq 5$ . As a numerical illustration, next we apply our theory to a one-dimensional two-band model, and benchmark its results with the DMRG simulations.

### III. NUMERICAL ILLUSTRATION

Our theoretical analysis given above is valid for both attractive ( $U < 0$ ) and repulsive ( $U > 0$ ) interactions. However, given the symmetry of the Bloch bands, i.e., see below for  $\varepsilon_{sk}(t, t') = -\varepsilon_{sk}(-t, -t')$ , and that of the Bose-Hubbard Hamiltonian, i.e.,  $H(t, t', U) = -H(-t, -t', -U)$ , below we consider only  $U < 0$ , since we are typically interested in the lowest-energy bound states that are below the continuum dissociation thresholds. That is our lowest-energy bound states for the  $U < 0$  case correspond to the highest-energy bound-states above the continuum thresholds when  $U > 0$ .

#### A. Sawtooth Lattice

For simplicity here we choose a sawtooth lattice that features two Bloch bands in the first BZ (say  $s = \{+, -\}$  bands) due to its  $N_b = 2$  sublattice sites in a unit cell (say  $S = \{A, B\}$  sublattices). We allow hopping between nearest-neighbor sites only, and set  $t_{A;Ai} = -t$  with  $j = i \pm 1$  and  $t \geq 0$ ,  $t_{B;Bi} = 0$  and  $t_{B;Ai} = t_{Bj;Ai} = -t'$  with  $j = i - 1$  and  $t' \geq 0$ . These are sketched in Fig. 1(b). The non-interacting Hamiltonian can be written as  $\mathcal{H}_0 = \sum_k \psi_k^\dagger (d_k^0 \sigma_0 + \mathbf{d}_k \cdot \boldsymbol{\sigma}) \psi_k$ , where  $\psi_k = (c_{Ak} \ c_{Bk})^T$  is a sublattice spinor,  $-\pi/a < k \leq \pi/a$  is in the first BZ with  $a$  the lattice spacing,  $d_k^0 = t \cos(ka)$ ,  $\sigma_0$  is a  $2 \times 2$

identity matrix,  $\mathbf{d}_k = (d_k^x, d_k^y, d_k^z)$  is a field vector with elements  $d_k^x = t' + t' \cos(ka)$ ,  $d_k^y = t' \sin(ka)$  and  $d_k^z = t \cos(ka)$ , and  $\boldsymbol{\sigma} = (\sigma_x, \sigma_y, \sigma_z)$  is a vector of Pauli spin matrices. The dispersion of the Bloch bands and the sublattice projections of the corresponding Bloch states can be written as

$$\varepsilon_{sk} = d_k^0 + sd_k, \quad (13)$$

$$s_{Ak} = \frac{-d_k^x + id_k^y}{\sqrt{2d_k(d_k - sd_k^z)}}, \quad (14)$$

$$s_{Bk} = \frac{d_k^z - sd_k}{\sqrt{2d_k(d_k - sd_k^z)}}, \quad (15)$$

where the index  $s = \pm$  denotes the upper and lower bands, respectively, and  $d_k$  is the magnitude of  $\mathbf{d}_k$ . Note that the lower band  $\varepsilon_{-,k} = -2t$  is flat and dispersionless when  $t'/t = \sqrt{2}$ . This is shown in Fig. 1(a). In addition one can recover the usual linear-chain model [8] by setting  $t = 0$ , however with the caveat that its single cosine-band appears as two bands in our BZ. This is because the usual BZ  $(-\pi/a_u, \pi/a_u]$  is folded into half  $(-\pi/a, \pi/a]$  for our lattice spacing  $a = 2a_u$ , leading to two bands that are symmetric around zero energy and no band gap in between.

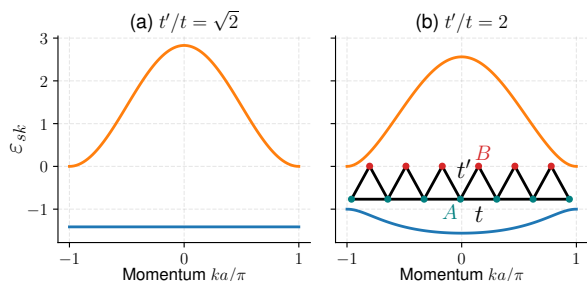


FIG. 1. Bloch bands  $\varepsilon_{sk}$  in a sawtooth lattice in the first BZ for (a)  $t = t'/\sqrt{2}$  and (b)  $t = t'/2$ . Hopping parameters are also sketched in (b). Lower band is completely flat in (a) where  $\varepsilon_{-,k} = -\sqrt{2}t' \approx -1.414t'$ . Ground-state energy is  $(1 - \sqrt{17})t'/2 \approx -1.561t'$  in (b).

## B. Two-body spectrum

The simplest bound states are those of the two-boson dimers that are determined by Eq. (8). However, since Eq. (8) is formally identical to that of the two-fermion case, we skip their detailed analysis here and refer the reader to the recent literature [2, 3]. Just like the fermion problem, it can be shown that, by representing Eq. (8) as an  $N_b \times N_b$  matrix equation for the  $\gamma_S(\mathbf{q})$  parameters, there are  $N_b$  distinct  $E_2^{\mathbf{q}}$  bound states for a given  $\mathbf{q}$ . In the sawtooth lattice the lower and upper dimer branches are associated, respectively, with the symmetric and antisymmetric combinations of the underlying sublattice contributions to the two-body wave function but

with different weights [2, 14]. The solutions are shown in Figs. 2(d) and 2(f), respectively, for  $t = t'/\sqrt{2}$  and  $t = t'/2$  as a function of  $q$  when  $U = -10t'$ . Note that these dimer branches appear at the bottom of the two-body spectrum, and they are well-separated from the rest of the states in the energy band.

Starting with the usual single-band linear-chain lattice in the  $t/t' \rightarrow 0$  limit which features a single dimer branch in its usual BZ [5], their doubling here in the sawtooth lattice can be traced back to doubling of the lattice spacing upon  $t/t' \neq 0$  and folding of the usual BZ. For instance in the flat-band case when  $t = t'/\sqrt{2}$ , the lower (upper) dimer branch has a bandwidth of  $0.43t'$  ( $0.20t'$ ), and its ground state  $-10.85t'$  ( $-10.37t'$ ) is located at the origin (edge)  $q = 0$  ( $q = \pi/a$ ) of the BZ. Likewise in the dispersive case when  $t = t'/2$ , the bandwidth  $0.36t'$  ( $0.28t'$ ) and ground state  $-10.77t'$  ( $-10.38t'$ ) are comparable. These are the so-called *onsite* dimers since their binding energies depend strongly on  $U$ , approaching eventually to  $U$  (with respect to the monomer-monomer continuum (i) discussed below) in the strong-coupling ( $U/t' \rightarrow -\infty$ ) limit. Note that there are two distinct onsite dimer branches in the sawtooth model since two bosons can be co-localized on one of the two sublattices. In addition the corresponding bandwidths ( $E_1$  and  $E_2$ ), and the band gap ( $\Delta$ ) of these dimer branches are shown in Fig. 3 as a function of  $U/t'$ . Altogether these results clearly show that the presence of a flat band does not make much impact on the onsite dimers, i.e., they have a sizeable dispersion at finite  $U$  in general. This is because the introduction of an additional infinitely-massive flat-band monomer reduces the effective band mass of the resultant dimers from its bare value (which is infinite at  $U = 0$ ) to a dressed one (which is finite at finite  $U$ ) through interband processes [2, 14, 16]. It is a somewhat counter-intuitive effect triggered by interactions in the presence of multiple Bloch bands. The effective band mass of the onsite dimers is also known to exhibit a dip in the weak-coupling regime, and then it increases for stronger couplings leading to a more and more localized onsite dimer in space.

Furthermore, in order to reveal the full two-body spectrum, here we recast Eq. (8) as an eigenvalue problem in terms of the original variational parameters, i.e.,

$$(\varepsilon_{n_1\mathbf{k}_1} + \varepsilon_{n_2,\mathbf{q}-\mathbf{k}_1} - E_2^{\mathbf{q}})\alpha_{n_1n_2}^{\mathbf{k}_1}(\mathbf{q}) = -\frac{U}{N_c} \sum_{n'_1n'_2\mathbf{k}_S} n_{1S\mathbf{k}_1}^* n_{2S,\mathbf{q}-\mathbf{k}_1}^* n'_{2S,\mathbf{q}-\mathbf{k}} n'_{1S\mathbf{k}} \alpha_{n'_1n'_2}^{\mathbf{k}}(\mathbf{q}), \quad (16)$$

and solve for  $E_2^{\mathbf{q}}$ . For a given  $\mathbf{q}$ , the solutions of Eq. (16) require numerical diagonalization of a matrix whose size grows as  $N_b^2 N_c$ , and we typically choose  $N_c = 100$  mesh points in the BZ in our two-body calculations. The results are shown in Figs. 2(a) and 2(b), respectively, for  $t = t'/\sqrt{2}$  and  $t = t'/2$  as a function of  $q$  when  $U = -10t'$ . We also checked that (not shown) our results reduce to that of the usual linear-chain model when  $t = 0$  [5]. In both figures it is easy to characterize the entire two-body



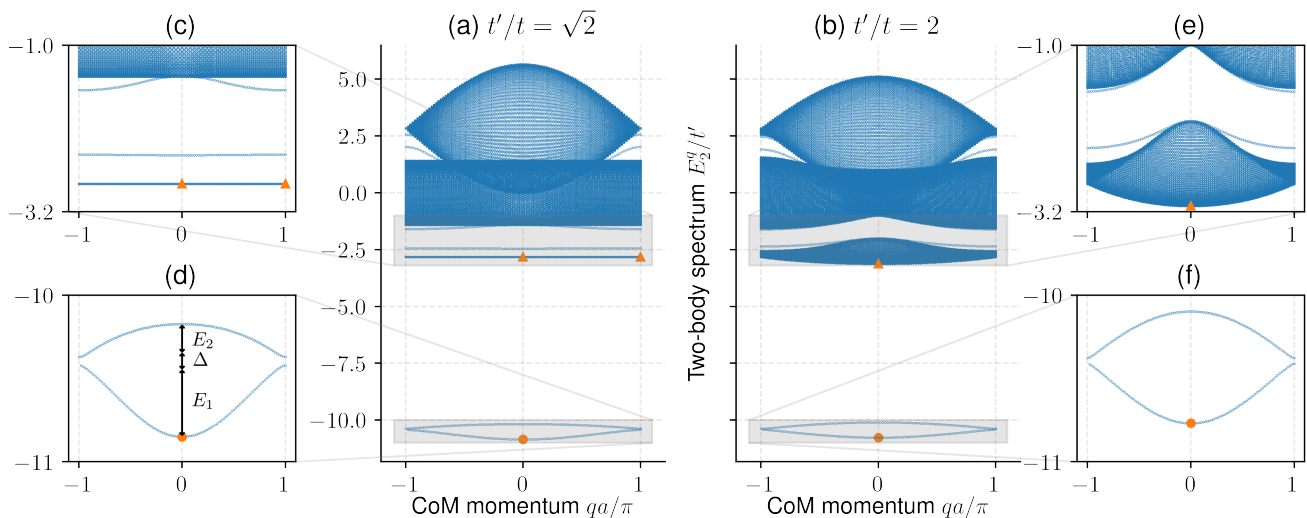


FIG. 2. Two-body spectrum  $E_2^q$  of the attractive ( $U = -10t'$ ) Bose-Hubbard model in a sawtooth lattice for  $t = t'/\sqrt{2}$  (left column) and  $t = t'/2$  (right column). Insets (d) and (f) are zooms to the lower and upper onsite dimer branches. Their bandwidths  $E_1$  and  $E_2$ , and the band gap  $\Delta$  in between are shown in Fig. 3 as a function of  $U/t'$ . Insets (c) and (e) are zooms to the monomer-monomer continua (i) and (ii), and two distinct offsite dimer branches in between. In (c) all of the continuum (i) states appear precisely at  $-2\sqrt{2}t' \approx -2.83t'$ , and the lower offsite dimer branch is around  $-2.45t'$ . Benchmarks with DMRG ground states for  $\rho_{max} = 2$  and  $\rho_{max} = 1$  are shown, respectively, with orange-colored markers  $\bullet$  and  $\blacktriangle$ .

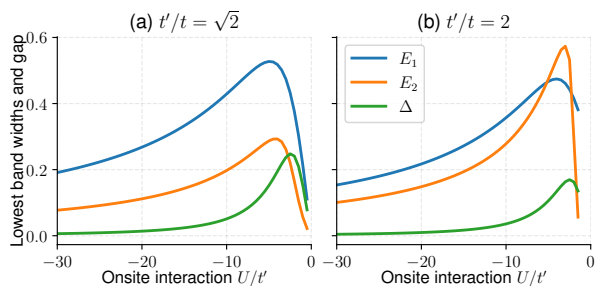


FIG. 3. Bandwidths  $E_1$  and  $E_2$ , and band gap  $\Delta$  of the onsite dimer branches shown in Figs. 2(d) and 2(f). These parameters play direct roles in the dimer-monomer continua shown in Figs. 4(d) and 4(f).

continuum which has contributions from three distinct monomer-monomer continua. Starting with the lowest one in energy, these are identified by the occupation of (i) two bosons in the lower Bloch band, (ii) one boson in the upper Bloch band and one boson in the lower Bloch band, and (iii) two bosons in the upper Bloch band. More importantly we find two additional dimer branches appearing in between the two consecutive continua. These are the so-called *offsite* dimers since their binding energies depend weakly on  $U$ , leading eventually to a small constant in the  $U/t' \rightarrow -\infty$  limit depending only on  $t/t'$ . These dimers consist of a monomer on one site and a monomer on another site even in the  $U/t' \rightarrow -\infty$  limit, i.e., the closest the two monomers can be is on nearest-neighbor sites. Such states do not appear in a single-band linear-chain model [5] since there is only a single monomer-monomer continuum there [17]. For

instance in the flat-band case when  $t = t'/\sqrt{2}$ , while the continuum (i) is located precisely at  $-2\sqrt{2}t'$ , the offsite dimer branch above this continuum has a small bandwidth of  $0.007t'$ , and its ground state  $-2.45t'$  is located at the origin  $q = 0$  of the BZ. These are illustrated in Fig. 2(c). Note that the effective band mass of the lower offsite dimer branch is much larger in magnitude than those of the onsite dimer branches. The continuum (ii) states occupy a rectangular region in Fig. 2(a) around zero energy because, for every monomer state in the upper Bloch band, there always exists a monomer state in the flat band whose total momenta add up to  $q$ , and this is possible for any given  $q$ . Thus the bandwidth of the continuum (ii) states is determined by the bandwidth of the upper Bloch band shown in Fig. 3(a).

In the next section, we show that the entire two-body spectrum, i.e., the two-body continua together with the onsite and offsite dimer branches, play equally important roles in the characterization of the three-body spectrum.

### C. Three-body spectrum

The three-body bound states can be determined by the integral Eq. (9) through an iterative procedure [3]. Instead, in order to reveal the full three-body spectrum, where we recast Eq. (9) as an eigenvalue problem in terms

of the original variational parameters, i.e.,

$$\begin{aligned}
& (\varepsilon_{n_1\mathbf{k}_1} + \varepsilon_{n_2\mathbf{k}_2} + \varepsilon_{n_3\mathbf{k}_3} - E_3^{\mathbf{q}}) \alpha_{n_1 n_2 n_3}^{\mathbf{k}_1 \mathbf{k}_2}(\mathbf{q}) = \quad (17) \\
& - \frac{U}{N_c} \sum_{n'_2 n'_3 \mathbf{k} S} n_{2S\mathbf{k}_2}^* n_{3S\mathbf{k}_3}^* n'_{3S, \mathbf{q}-\mathbf{k}_1-\mathbf{k}} n'_{2S\mathbf{k}} \alpha_{n_1 n'_2 n'_3}^{\mathbf{k}_1 \mathbf{k}}(\mathbf{q}) \\
& - \frac{U}{N_c} \sum_{n'_1 n'_3 \mathbf{k} S} n_{1S\mathbf{k}_1}^* n_{3S\mathbf{k}_3}^* n'_{3S, \mathbf{q}-\mathbf{k}_2-\mathbf{k}} n'_{1S\mathbf{k}} \alpha_{n'_1 n_2 n'_3}^{\mathbf{k} \mathbf{k}_2}(\mathbf{q}) \\
& - \frac{U}{N_c} \sum_{n'_1 n'_2 \mathbf{k} S} n_{1S\mathbf{k}_1}^* n_{2S\mathbf{k}_2}^* n'_{2S, \mathbf{q}-\mathbf{k}_3-\mathbf{k}} n'_{1S\mathbf{k}} \alpha_{n'_1 n'_2 n_3}^{\mathbf{k}, \mathbf{q}-\mathbf{k}_3-\mathbf{k}}(\mathbf{q}),
\end{aligned}$$

and solve for  $E_3^{\mathbf{q}}$ . Recall that  $\mathbf{k}_3 = \mathbf{q} - \mathbf{k}_1 - \mathbf{k}_2$  when  $N = 3$ , and note that the exchange-symmetry constraints are imposed on the variational parameters by construction. For a given  $\mathbf{q}$ , the solutions of Eq. (17) require numerical diagonalization of large matrices whose size grows as  $N_b^3 N_c^2$ , and we typically choose  $N_c = 50$  mesh points in the BZ in our three-body calculations. Decreasing it to  $N_c = 40$  makes only minor changes. Since our numerical recipe follows closely that of the (3+1)-body problem, i.e., three spin- $\uparrow$  fermions and one spin- $\downarrow$  fermion, that we recently introduced for the four-fermion case [4], we skip its details here. The results are shown in Figs. 4(a) and 4(b), respectively, for  $t = t'/\sqrt{2}$  and  $t = t'/2$  as a function of  $q$  when  $U = -10t'$ . We also checked that (not shown) our results reduce to that of the usual linear-chain model when  $t = 0$  [8]. In both figures the spectrum splits into three groups of states, i.e., starting with the lowest one in energy: (I) two trimer branches lie around  $3U$  for a given  $q$ , (II) dimer-monomer continua are packed around  $U$ , and (III) monomer-monomer-monomer continua are packed around zero energy. The group (I) branches are best resolved in the corresponding lowest-energy solutions (first ten of them) that are shown in Figs. 5(a) and 5(b) as a function of  $U/t'$  at  $q = \pi/a$ .

First of all, similar to the two-body spectrum, we find that there are two trimer branches appearing at the bottom of the three-body spectrum, and they are well-separated from the rest of the states in the spectrum. Starting with the usual single-band linear-chain lattice in the  $t/t' \rightarrow 0$  limit which features a single trimer branch in its usual BZ [8], their doubling here in the sawtooth lattice can again be traced back to doubling of the lattice spacing upon  $t/t' \neq 0$  and folding of the usual BZ. These are the so-called *onsite* trimers since their binding energies depend strongly on  $U$ , approaching eventually to  $2U$  (with respect to the dimer-monomer continua) in the  $U/t' \rightarrow -\infty$  limit [1, 8]. We again note that there are two distinct onsite trimer branches in the sawtooth model since three bosons can be co-localized on one of the two sublattices. Unlike the highly dispersive onsite dimer branches, the onsite trimer branches have nearly-flat dispersions even in the weak-binding low- $U/t'$  regime, i.e., since the effective band mass of the onsite trimers is much larger in magnitude than that of the onsite dimers, the onsite trimers are more localized in space. For instance in the flat-band case when  $t = t'/\sqrt{2}$ , the

lower (upper) onsite trimer branch has a small bandwidth of  $0.011t'$  ( $0.0047t'$ ), and its ground state  $-30.4379t'$  ( $-30.2911t'$ ) is located at the edge  $q = \pi/a$  of the BZ. Their energy difference fits very well with  $(\sqrt{2}t'/U)t'$  in the strong-coupling up to low  $U/t' \sim -3$  values. Likewise in the dispersive case when  $t = t'/2$ , the bandwidth  $0.0046t'$  ( $0.0094t'$ ) is again small but the ground state  $-30.3682t'$  ( $-30.2939t'$ ) is located at the origin  $q = 0$  (edge  $q = \pi/a$ ).

At the bottom of group (II) states, there are the so-called *offsite* trimers since their binding energies depend weakly on  $U$ , leading eventually to a small constant (with respect to the dimer-monomer continua) in the  $U/t' \rightarrow -\infty$  limit depending only on  $t/t'$ . These trimers consist of a dimer on one site and a monomer on another site even in the  $U/t' \rightarrow -\infty$  limit, i.e., the closest the dimer and the monomer can be is on nearest-neighbor sites. These states are shown in Figs. 4(d) and 4(f). For instance in the flat-band case when  $t = t'/\sqrt{2}$ , the lowest offsite trimer branch has a small bandwidth of  $0.0096t'$ , and its ground state  $-13.2256t'$  is located at the edge  $q = \pi/a$  of the BZ. Likewise in the dispersive case when  $t = t'/2$ , its bandwidth  $0.065t'$  is also small but its ground state  $-13.0015t'$  is located at  $q = \pi/a$ . Thus the effective band mass of the lowest offsite trimers is also much larger in magnitude than that of the onsite dimers. Unlike the offsite dimers which appear only in the presence of multiple bands, these offsite trimers are known to appear also in a single-band linear-chain model but when  $U$  is sufficiently strong. However, while there appears precisely a single trimer branch in the single-band model [8], here we observe several branches in a two-band model whose number depends strongly on  $U/t'$  [18]. Note that the gradual appearance of additional offsite trimer branches with increasing  $U/t'$  is clearly seen in Fig. 5. In addition the lowest trimer branch emerges from the dimer-monomer continuum continuously in the flat-band case without a threshold on  $U$ , which is signalled by the apparent nondegeneracy of the third eigenvalue for all  $U/t'$  in Fig. 5(a).

Furthermore the group (II) states have contributions from four distinct dimer-monomer continua. Starting with the lowest one in energy (which assumes  $U/t'$  is sufficiently strong), these are identified by the occupation of (II-a) two bosons in the lower onsite dimer branch and one boson in the lower Bloch band, (II-b) two bosons in the upper onsite dimer branch and one boson in the lower Bloch band, (II-c) two bosons in the lower onsite dimer branch and one boson in the upper Bloch band, and (II-d) two bosons in the upper onsite dimer branch and one boson in the upper Bloch band. For instance the first continuum (II-a) first appears around  $-10.85t' - 1.41t' = -12.26t'$  and  $-10.77t' - 1.56t' = -12.33t'$ , respectively, when  $t = t'/\sqrt{2}$  and  $t = t'/2$ . These are shown in Figs. 4(d) and 4(f). In the particular case when the lower Bloch band is flat, the bandwidths of continuum (II-a) and continuum (II-b) are determined, respectively, by solely the bandwidths ( $E_1$  and  $E_2$ ) of the lower and

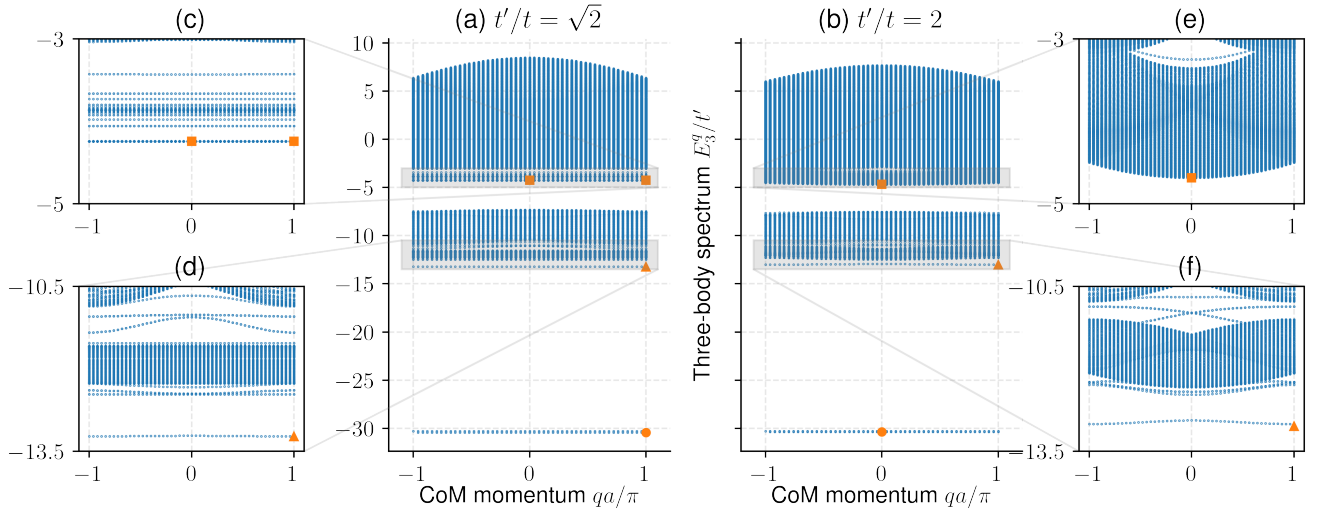


FIG. 4. Three-body spectrum  $E_3^q$  of the attractive ( $U = -10t'$ ) Bose-Hubbard model in a sawtooth lattice for  $t = t'/\sqrt{2}$  (left column) and  $t = t'/2$  (right column). Insets (d) and (f) are zooms to the offsite trimer branches nearby the dimer-monomer continua (II-a), (II-b) and (II-c). Insets (c) and (e) are zooms to the monomer-monomer-monomer continua (III-a) and (III-b), and the offsite trimer branches and offsite-dimer-monomer continua in between. In (c) all of the continuum (III-a) states appear precisely at  $-3\sqrt{2}t' \approx -4.24t'$ , and the origin of the continuum of states around  $-2.45t' - \sqrt{2}t' \approx -3.86t'$  can be traced back to the lower offsite dimer branch shown in Fig. 2(c) around  $-2.45t'$ . Benchmarks with the DMRG ground states for  $\rho_{max} = 3$ ,  $\rho_{max} = 2$  and  $\rho_{max} = 1$  are shown, respectively, with orange-colored markers  $\bullet$ ,  $\blacktriangle$  and  $\blacksquare$ .

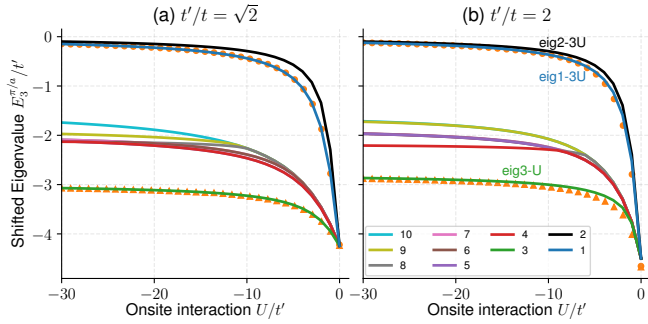


FIG. 5. Lowest ten eigenvalues  $E_3^{\pi/a}$  at  $q = \pi/a$  for (a)  $t = t'/\sqrt{2}$  and (b)  $t = t'/2$ . First three of them belong, respectively, to the lower onsite trimer, upper onsite trimer and the lowest offsite trimer branches. Note that the latter branch emerges from the dimer-monomer continuum (II-a) continuously (discontinuously) in the flat-band (dispersive-band) case without (with) a threshold on  $U$ . In (b) this threshold is signalled by the apparent degeneracy of the third eigenvalue with the rest (fourth, fifth, sixth, etc.) at low  $U/t'$ . Onsite trimer energies are shifted by  $3U$  but the rest are shifted by  $U$  for convenience. Benchmarks with the DMRG ground states for  $\rho_{max} = 3$  and  $\rho_{max} = 2$  are shown, respectively, with orange-colored markers  $\bullet$  and  $\blacktriangle$ .

upper onsite dimer branches that are shown in Fig. 3(a). Note that the gap between continuum (II-a) and continuum (II-b) is determined by  $\Delta$ , and it is barely visible here. In both figures we also find several additional offsite trimer branches in between the continuum (II-b) and continuum (II-c). There is also an additional offsite trimer branch above the continuum (II-d) which is not visible

in the shown scale.

Likewise the group (III) states have contributions from four distinct unbound monomer-monomer-monomer continua. Starting with the lowest one in energy, these are identified by the occupation of (III-a) three bosons in the lower Bloch band, (III-b) two boson in the lower Bloch band and one boson in the upper Bloch band, (III-c) one boson in the lower Bloch band and two bosons in the upper Bloch band, and (III-d) three bosons in the upper Bloch band. For instance the first continuum (III-a) appears at  $-3\sqrt{2}t' \approx -4.24t'$  and  $3(1-\sqrt{17})t'/2 \approx -4.68t'$ , respectively, when  $t = t'/\sqrt{2}$  and  $t = t'/2$ . These are shown in Figs. 4(c) and 4(e). In our numerical calculations, we did not find any offsite trimer branch below the continuum (III-a). However, there can be offsite trimer branches in between continuum (III-a) and continuum (III-b). For instance these branches are clearly seen in the flat-band case when  $t = t'/\sqrt{2}$ . Right above them we also find a continuum of states that are packed around  $-2.45t' - \sqrt{2}t' \approx -3.86t'$ . These are shown in Fig. 4(c). It turns out the latter can be identified as an additional dimer-monomer continuum, emerging from the occupation of the lower offsite dimer branch that we found at  $-2.45t'$  in Fig. 2(c) and a monomer in the flat Bloch band. These states consist of three monomers that can at most be found on different nearest-neighbor sites even in the  $U/t' \rightarrow -\infty$  limit. Furthermore while the continuum (III-b) is expected to appear at  $-2\sqrt{2}t' + 0t' \approx -2.83t'$  in the flat-band case, we find a continuum of states starting around  $-3.00t'$ , which is barely visible at the top of Fig. 4(c). This is because there is yet another dimer-monomer continuum emerging from the occupation of

the upper offsite dimer branch that we found right below the monomer-monomer continuum (iii) in Fig. 2(c) and a monomer in the flat Bloch band.

Having analyzed the two-body and three-body spectra for the sawtooth lattice via our exact variational results, next we benchmark them with the DMRG simulations.

#### D. DMRG Simulations

Even though one can understand much of the two-body spectrum by looking at the Bloch bands alone, and in return can also keep track a large portion of the three-body spectrum by looking at the two-body spectrum, it is important to benchmark and verify our results with an independent calculation. Here we present our numerically-exact DMRG simulations [19–21] on a large lattice with up to  $N_c = 100$  unit cells. Our checks include not only the ground states of the two-body and the three-body spectra (i.e., the ground states for the lower onsite dimer branches shown in Figs. 2(d) and 2(f), and for the lower onsite trimer branches shown in Figs. 4(a) and 4(b), respectively) but also the ground states for the offsite trimer branches that are shown in Figs. 4(d) and 4(f). While the former is achieved by allowing a large cutoff in the local Hilbert space (i.e., local number of bosons) on each lattice site (i.e., any  $\rho_{max} \geq 3$  is sufficient for the onsite trimers), the latter is achieved through restricting  $\rho_{max} = 2$  to that of an onsite dimer. Setting  $\rho_{max} = 1$  determines the bottom edge of the continuum (III-a).

In the flat-band case when  $t = t'/\sqrt{2}$ , we note that the agreement between the variational approach and the DMRG simulations is almost perfect, i.e., the relative accuracy between the two is typically better than 0.1% for all of the parameters that we considered. Setting  $\rho_{max} = 2$  works surprisingly well for the offsite trimers because the flat-band dimers are already in the strong-coupling limit when they first form at arbitrarily weak  $U \neq 0$ . However, in the dispersive case when  $t = t'/2$ , while the agreement is again almost perfect for the onsite trimers, it is not as good for the offsite trimers when  $U/t' \gtrsim -10$  is relatively weak. This shows that  $\rho_{max} = 2$  provides only a qualitatively accurate description (but not a quantitative one) for the offsite trimers in the weak-coupling regime. Thus our successful benchmark for the strong-coupling  $U/t' \rightarrow -\infty$  limit suggests that the states in the lowest offsite trimer branch can really be thought of a bound state between an onsite dimer and a monomer occupying different lattice sites, and hence the origin of their name *offsite*. Note that a similar strategy does not work for the ground states of the offsite dimer branches that are shown in Figs. 2(c) and 2(e), since they appear above the monomer-monomer continuum (i) but not below it, i.e., setting  $\rho_{max} = 1$  determines the bottom edge of the continuum (i).

Given our almost perfect benchmark for the ground states of onsite dimers, onsite trimers and offsite trimers, we also perform DMRG simulations for the onsite

tetramers, offsite tetramers, onsite pentamers, offsite pentamers, etc. That is we study the ground states of various  $N$ -body multimers by setting  $\rho_{max} = \{N, N - 1, \dots, 2\}$  for a given  $N$ . These results are shown in Fig. 6. For a given  $N = \{4, 5, 6\}$  and  $\rho_{max}$ , the DMRG simulation gives the ground state energy for the multimer that has at most  $\rho_{max}$  particles on a given site. As shown in Fig. 6, the ground-state energy  $E_N(\rho_{max})$  of the corresponding multimer generally approaches to

$$E_{sat} = n \frac{\rho_{max}(\rho_{max} - 1)}{2} U + \frac{m(m - 1)}{2} U \quad (18)$$

in the strong-coupling limit, where the integers  $n \geq 0$  and  $0 \leq m < \rho_{max}$  are such that  $N = n\rho_{max} + m$ . This is because, for a given  $\rho_{max}$ , the ground state of the offsite  $N$ -body multimer consists of  $n$  onsite  $\rho_{max}$ -body multimers and an onsite  $m$ -body multimer that are all on different sites. For instance while the  $\rho_{max} = N$  case recovers the expected ground state of the onsite  $N$ -body multimer that is strongly localized on a single lattice site [1], the  $\rho_{max} = N - 1$  case gives the ground state of the offsite  $N$ -body multimer that consists of at most an onsite  $(N - 1)$ -body multimer on one site and a monomer on another site. Setting  $\rho_{max} = 1$  generally determines the bottom edge of the continuum that is characterized by  $N$  unbound (non-interacting) monomers in the lowest Bloch band.

Our numerical results confirm that the binding energy of the onsite  $N$ -body multimers increases with  $N$  and  $U$  without a bound, i.e., it trivially goes as  $E_b = -E_N(N) + E_{N-1}(N-1) + E_1(1) \approx -(N-1)U$  in the strong-coupling limit. Therefore, similar to the onsite dimers and onsite trimers, we expect the effective band mass of all onsite  $N$ -body multimers to increase in the strong-coupling regime, where these states become more and more localized in space. In addition the larger the size  $N$  of the onsite multimer, the higher its effective band mass is for a given  $U$ .

More importantly our results also suggest that the binding energy of the lowest offsite  $N$ -body multimers can generally be defined as

$$E_b = -E_N(N - 1) + E_{N-1}(N - 1) + E_1(1) \quad (19)$$

in the strong-coupling limit. Furthermore this definition is expected to be valid for all  $N$  and  $U$  in the flat-band case, since the onsite multimers there are already in the strong-coupling limit when they first form at arbitrarily weak  $U \neq 0$ . In fact we checked this for low- $N$  values by considering all other possible dissociation processes, and verified that Eq. (19) gives the largest binding energy. For instance  $E_b$  corresponds precisely to the energy gap between the lowest offsite trimer branch and the dimer-monomer continuum (II-a) that are shown in Fig. 4(d). Our DMRG results are shown in Fig. 6(d) as a function of  $U/t'$  for  $N = \{3, 4, 5, 6\}$ . For the offsite trimers with  $N = 3$ ,  $E_b$  increases monotonously from 0 to a constant value in the strong-coupling limit, signalling that



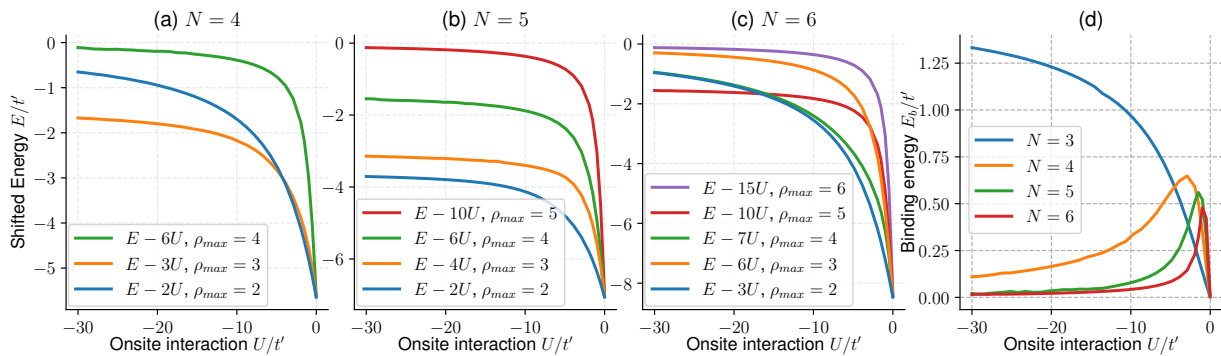


FIG. 6. DMRG ground-state energy  $E_N(\rho_{max})$  for (a) the tetramer ( $N = 4$ ), (b) pentamer ( $N = 5$ ), and (c) hexamer ( $N = 6$ ) states in a flat band (i.e.,  $t = t'/\sqrt{2}$ ) when the local number of bosons is restricted to  $\rho_{max} = \{N, N - 1, \dots, 2\}$ . The energies are shifted by  $E_{sat}$  for convenience. Since the ground states for the dispersive case (i.e.,  $t = t'/2$ ) are quantitatively very similar, they are not shown. Binding energy  $E_b$  for the lowest offsite  $N$ -body multimers are shown in (d).

the onsite dimer and the monomer are eventually on the nearest-neighbor sites. Similar to the usual linear-chain model [8], their binding mechanism is expected to be an effective particle-exchange interaction which depends only on the hopping parameters  $t/t'$  but not on  $U$ . This is because the exchange process  $|2, 1\rangle \rightarrow |1, 2\rangle$  does not involve  $U$ . On the other hand, for larger offsite multimers with  $N \geq 4$ ,  $E_b$  first exhibits a peak in the weak-coupling regime and then it decays for stronger couplings. This indicates that the effective particle-exchange interaction between the constituents of the offsite  $N$ -body multimer, i.e., the  $|N - 1, 1\rangle \rightarrow |N - 2, 2\rangle$  process between the onsite  $(N - 1)$ -body multimer and the monomer, not only depends on  $U$  but also decreases in the strong-coupling regime. This is because, given that increasing the coupling strength strongly localizes the onsite  $(N - 1)$ -body multimer state in space (i.e., increases both of its binding energy and effective band mass), it becomes energetically more difficult to exchange one of its constituents with the monomer on another site due to decreasing overlap of their wave functions. This also explains why  $E_b$  decays faster for larger  $N$ .

#### IV. CONCLUSION

In summary here we derived exact integral equations for the dimers, trimers, tetramers, and other multimers that are described by a multiband Bose-Hubbard model with generic hoppings and an onsite attractive interaction. As an illustration, we calculated the two-body and three-body spectra in a sawtooth model, and revealed the presence of both the weakly-bound offsite dimer states which consist of two monomers on different sites even in

the strong-coupling ( $U/t' \rightarrow -\infty$ ) limit, and the weakly-bound offsite trimer states which consist of either a dimer on one site and a monomer on another site or three monomers on three different sites. We benchmarked the ground states of onsite dimers, onsite trimers and offsite trimers with the DMRG simulations, and presented additional DMRG results for the ground states of onsite tetramers, offsite tetramers, onsite pentamers, offsite pentamers and for those of other multimers.

Even though we restricted our numerical analysis here to a one-dimensional model, i.e., due mainly to our benchmarking capacity with the DMRG simulations, our variational results may find practical applications in future few-body studies, since they are readily applicable to all sorts of lattices in all dimensions. As an outlook it may be useful to develop a simpler effective model that reveals the binding mechanism of offsite  $N$ -body multimers in the presence of multiple bands. It is expected to be very similar to that of the offsite trimers in a single-band lattice [8], i.e., there must be an effective particle-exchange interaction between an onsite  $(N - 1)$ -body multimer on one site and a monomer on another site, between an onsite  $(N - 2)$ -body multimer on one site and a dimer on another site, between an onsite  $(N - 2)$ -body multimer on one site and two monomers on two other sites, etc.

#### ACKNOWLEDGMENTS

We thank M. Valiente for his comments and suggestions. A. K. is supported by TÜBİTAK 2236 Co-funded Brain Circulation Scheme 2 (CoCirculation2) Project No. 120C066.

[1] D. C. Mattis, The few-body problem on a lattice, *Rev. Mod. Phys.* **58**, 361 (1986).

[2] G. Orso and M. Singh, Pairs, trimers, and BCS-BEC crossover near a flat band: Sawtooth lattice, *Phys. Rev.*

- B **106**, 014504 (2022).
- [3] M. Iskin, Three-body problem in a multiband Hubbard model, *Phys. Rev. A* **105**, 063310 (2022).
- [4] M. Iskin and A. Keleş, Few-body clusters in a multiband Hubbard model: Tetramers, pentamers, and beyond (2022), [arXiv:2204.10003](https://arxiv.org/abs/2204.10003).
- [5] M. Valiente and D. Petrosyan, Two-particle states in the Hubbard model, *Journal of Physics B: Atomic, Molecular and Optical Physics* **41**, 161002 (2008).
- [6] J. Javanainen, O. Odong, and J. C. Sanders, Dimer of two bosons in a one-dimensional optical lattice, *Phys. Rev. A* **81**, 043609 (2010).
- [7] J. C. Sanders, O. Odong, J. Javanainen, and M. Mackie, Bound states of two bosons in an optical lattice near an association resonance, *Phys. Rev. A* **83**, 031607 (2011).
- [8] M. Valiente, D. Petrosyan, and A. Saenz, Three-body bound states in a lattice, *Phys. Rev. A* **81**, 011601 (2010).
- [9] M. P. A. Fisher, P. B. Weichman, G. Grinstein, and D. S. Fisher, Boson localization and the superfluid-insulator transition, *Phys. Rev. B* **40**, 546 (1989).
- [10] M. Greiner, O. Mandel, T. Esslinger, T. W. Hänsch, and I. Bloch, Quantum phase transition from a superfluid to a Mott insulator in a gas of ultracold atoms, *Nature* **415**, 39 (2002).
- [11] I. B. Spielman, W. D. Phillips, and J. V. Porto, Condensate fraction in a 2d Bose gas measured across the Mott-insulator transition, *Phys. Rev. Lett.* **100**, 120402 (2008).
- [12] N. Gemelke, X. Zhang, C.-L. Hung, and C. Chin, In situ observation of incompressible Mott-insulating domains in ultracold atomic gases, *Nature* **460**, 995 (2009).
- [13] W. S. Bakr, A. Peng, M. E. Tai, R. Ma, J. Simon, J. I. Gillen, S. Foelling, L. Pollet, and M. Greiner, Probing the superfluid-to-Mott insulator transition at the single-atom level, *Science* **329**, 547 (2010).
- [14] M. Iskin, Two-body problem in a multiband lattice and the role of quantum geometry, *Phys. Rev. A* **103**, 053311 (2021).
- [15] P. Kornilovitch, A stable pair liquid phase in fermionic systems (2022), [arXiv:2204.02214](https://arxiv.org/abs/2204.02214).
- [16] M. Iskin, Effective-mass tensor of the two-body bound states and the quantum-metric tensor of the underlying Bloch states in multiband lattices, *Phys. Rev. A* **105**, 023312 (2022).
- [17] Since the lowest offsite dimer branch appears above the monomer-monomer continuum (i) but not below it, we suspect that their peculiar binding mechanism is mediated by an effective nearest-neighbor repulsion that is induced by the interband processes. This can be revealed by, e.g., following Ref. [8], and deriving an effective hardcore extended Bose-Hubbard Hamiltonian for the offsite dimers in the strong-coupling limit through an adiabatic elimination of the onsite dimers. We believe theoretical modelling of the binding mechanisms for the various offsite dimers, offsite trimers, offsite tetramers, etc., are interesting research problems by themselves, and are beyond the scope of this paper.
- [18] It turns out these offsite boson trimers are in many ways similar to the fermion trimers in the  $(2+1)$ -body problem [3]. For instance the fermion trimers are necessarily offsite and they are weakly-bound due to the Pauli exclusion principle preventing the formation of onsite trimers. What is astounding is that, in the case of sawtooth model, the low-energy spectrum of the  $(2+1)$ -body fermion problem coincides exactly (i.e., up to the machine precision) with excited states of the three-boson problem. Our variational calculations for the Hubbard and Bose-Hubbard models show that this is generally the case for any given set of  $\{t, t', U\}$ . It is such that the energy of the ground fermion trimer state coincides with the fifth lowest eigenvalue (i.e., third offsite trimer branch) of the boson one for any given CoM momentum  $q$ . In addition the energy of the excited fermion trimer state coincides with the seventh lowest eigenvalue (i.e., fifth offsite trimer branch) of the boson one. See the revised version of Ref. [4] for a more detailed comparison.
- [19] S. R. White, Density matrix formulation for quantum renormalization groups, *Phys. Rev. Lett.* **69**, 2863 (1992).
- [20] U. Schollwöck, The density-matrix renormalization group in the age of matrix product states, *Ann. Phys.* **326**, 96 (2011).
- [21] M. Fishman, S. R. White, and E. M. Stoudenmire, The ITensor software library for tensor network calculations (2020), [arXiv:2007.14822](https://arxiv.org/abs/2007.14822).